Clim Dyn (2007) 29:357–373
DOI 10.1007/s00382-007-0237-x

The effect of land surface changes on Eemian climate

Guy Schurgers · Uwe Mikolajewicz · Matthias Gröger · Ernst Maier-Reimer · Miren Vizcaíno · Arne Winguth

Received: 20 February 2006 / Accepted: 29 January 2007 / Published online: 9 March 2007

Abstract Transient experiments for the Eemian (128–113 ky BP) were performed with a complex, coupled earth system model, including atmosphere, ocean, terrestrial biosphere and marine biogeochemistry. In order to investigate the effect of land surface parameters (background albedo, vegetation and tree fraction and roughness length) on the simulated changes during the Eemian, simulations with interactive coupling between climate and vegetation were compared with additional experiments in which these feedbacks were suppressed. The experiments show that the influence of land surface on climate is mainly caused by changes in the albedo. For the northern hemisphere high latitudes, land surface albedo is changed partially due to the direct albedo effect of the conversion of grasses into forest, but the indirect effect of forests on snow albedo appears to be the major factor influencing the total absorption of solar radiation. The Western Sahara region experiences large changes in land surface albedo due to the appearance of vegetation between 128 and 120 ky BP. These local land surface albedo changes can be as much as 20%, thereby affecting the local as well as the global energy balance. On a global scale, latent heat loss over land increases more than 10% for 126 ky BP compared to present-day.

G. Schurgers (✉) · U. Mikolajewicz · M. Gröger · E. Maier-Reimer · M. Vizcaíno
Max Planck Institute for Meteorology, Bundesstrasse 53, 20146 Hamburg, Germany
e-mail: guy.schurgers@nateko.lu.se

Present Address:
G. Schurgers
Department of Physical Geography and Ecosystems Analysis, Lund University, Sölvegatan 12, 223 62 Lund, Sweden

Present Address:
M. Vizcaíno
Department of Geography, University of California, 531 McCone Hall, Berkeley, CA 94720-4740, USA

A. Winguth
Department of Atmospheric and Oceanic Sciences, Center for Climatic Research, 1225 W. Dayton St, Madison, WI 53706, USA

1 Introduction

The effect of land surface changes on climate has long been excluded from climate model experiments. Growing awareness of the importance of land surface for climate resulted from a number of studies with changes in land surface conditions: first to study the sensitivity of a model to these changes, later to quantify the importance of realistic land surface changes for climate. Many of the studies were performed with paleoclimatic settings, because of the remarkable changes for the land surface that have been recorded for the past (e.g. as reported by Prentice and Webb III 1998). The overview below briefly illustrates the richness of types of previous studies, and tries to group them by the approach used for studying the land surface effects.

Many studies were performed considering the importance of taiga and tundra in the high latitudes, starting with experiments prescribing albedo changes by Otterman et al. (1984). In later studies, deforestation was usually prescribed for certain regions (e.g. Bonan et al. 1992; Thomas and Rowntree 1992; Douville and Royer 1997). Experiments were performed as well for the Mid-Holocene (6 ky BP) prescribing forest expansion in the north (e.g. Foley et al. 1994; TEMPO 1996), as was reported from proxy

data for this epoch. These studies usually focus on the enhancement of the climate effect of prescribed insolation changes due to a biogeophysical feedback from the land surface: expansion of forests causes a decrease of the land surface albedo, an increase of the amount of absorbed solar radiation and thereby an increase in temperature. On the one hand, this increase in temperature causes a decrease of the total snow covered area and a shortening of the duration of snow cover on the ground, thereby enhancing the albedo effect. On the other hand, the increase in temperature favours the growth of forests, which causes a positive feedback as well.

Later, paleoclimate reconstructions of lake levels and vegetation from proxy data were used to drive general circulation models (Coe and Bonan 1997; Crowley and Baum 1997; Diffenbaugh and Sloan 2002). This is a step in the direction of realistic modelling of the past and the effect of land surface changes can be estimated from the difference between these experiments and experiments with a present-day land surface, however feedbacks between land surface and climate are not simulated interactively.

To consider these feedbacks, simulated vegetation changes have been included in paleoclimate simulations and analysis (TEMPO 1996). The feedback between atmosphere and land surface was studied in the Sahara desert region with an equilibrium vegetation model iteratively coupled to a dynamic atmosphere model for the Mid-Holocene by Claussen (1997), Claussen and Gayler (1997), Texier et al. (1997), Claussen (1998) and de Noblet-Ducoudré et al. (2000). The greening of the Sahara desert was reported in many studies, and is closely linked to changes in the surface albedo. A decrease of surface albedo and increase of vegetation cover causes several associated effects that play a role in greening of the Sahara desert. A decrease of surface albedo and thus an increase in the absorption of shortwave radiation causes an increase in sensible and latent heat loss to the atmosphere. This additional energy in the atmosphere is balanced by an increase in ascending air and in convection (Charney 1975; Charney et al. 1975, 1976). The increase of moist static energy of the atmosphere near the surface enhances the circulation pattern, which promotes the transport of moisture into the North African continent (Eltahir 1996; Eltahir and Gong 1996; Claussen 1997; Braconnot et al. 1999). Besides these processes, the presence of vegetation might play an important role in soil moisture accessibility for evaporation and recycling of precipitation (De Ridder 1998). All these processes result in enhanced precipitation, which is the key limiting factor for plant growth in the Sahara region. These processes differ substantially in the spatial scale of explanation: some focus more on the local surface effects, whereas especially for the moisture transport regional effects are taken into account.

Later, the coupling was performed with more sophisticated models for the vegetation and land surface. Complex coupled atmosphere–vegetation models (or atmosphere–ocean–vegetation models) were used, which simulate the state of vegetation directly, and were usually applied for time slices of interesting epochs. The Last Glacial Maximum (21 ky BP) was studied by Levis et al. (1999) and Crucifix et al. (2005), the Mid-Holocene was studied by Gallimore et al. (2005). Some of the studies mentioned above took the role of decreased CO_2 concentration into account, e.g. for the Last Glacial Maximum (Crowley and Baum 1997; Levis et al. 2000; Crucifix et al. 2005).

Longer transient simulation of paleoclimatic time periods with earth system models are up to now only performed using intermediate complexity models (EMICs, Claussen et al. 2002), since the use of fully coupled atmosphere–ocean general circulation models is limited by the computational resources. Claussen et al. (1999) and Brovkin et al. (2002) used the CLIMBER-2 model to study the Holocene (from 9 ky BP to present), Calov et al. (2005) used the same model, now including ice sheets, to study the Eemian and the glacial inception (126–100 ky BP). The period between 126 and 115 ky BP was studied as well with the MoBidiC model by Crucifix and Loutre (2002). Performing longer transient simulations with atmosphere–ocean GCMs has so far only been done by accelerating the insolation forcing, e.g. as was done by Lorenz and Lohmann (2004).

For this study we performed transient simulations with a complex earth system model, instead of an intermediate complexity model. The earth system model consists of general circulation models for atmosphere and ocean, and models for the terrestrial biosphere and ocean biogeochemistry. The use of general circulation models enables a more comprehensive representation of weather and climate than given by EMICs. By using a rather coarse resolution, combined with a periodically-synchronous coupling technique (Sausen and Voss 1996), we were able to perform experiments with unaccelerated as well as accelerated insolation forcing for longer transient periods.

The aim of this paper is threefold: (1) to describe the parametrization of the biogeophysical land surface from the state of the vegetation, (2) to investigate the effect of insolation changes on climate, vegetation and land surface feedbacks and (3) to investigate the underlying mechanisms of these land surface feedbacks, and the importance of certain land surface parameters for these. The insolation effects and the underlying feedback mechanisms are studied for insolation changes during the last interglacial (Eemian). We chose this time period because it exhibits changes in the orbital forcing comparable to the Holocene, but due to a larger eccentricity of the earth's orbit, changes in climate as well as changes in vegetation and its feed-

backs are likely to be somewhat larger, especially during summer. This allows us to study the potential non-linearities in the climate–vegetation system over a wider range of insolation than would have been possible for the Holocene. In this paper we will focus on the biogeophysical effects of the vegetation on climate, the biogeochemistry is discussed in Schurgers et al. (2006).

2 Method

A coupled earth system model, consisting of atmosphere and ocean general circulation models, an ocean biogeochemistry model and a dynamic global vegetation model, was used to study the effect of changes in the land surface on the climate of the Eemian. The coupled atmosphere–ocean general circulation model ECHAM3-LSG, as used in Mikolajewicz and Voss (2000) and Voss and Mikolajewicz (2001), was improved and expanded with the dynamic global vegetation model LPJ (Sitch et al. 2003) and the ocean biogeochemistry model HAMOCC (Maier-Reimer 1993). The earth system model used here is the same as in Winguth et al. (2005) and Mikolajewicz et al. (2007), but the ice sheets are fixed at their present-day state. The CO_2 concentration is calculated prognostically from the fluxes between atmosphere, terrestrial biosphere and marine biogeochemistry.

The Lund–Potsdam–Jena dynamic global vegetation model (LPJ, Sitch et al. 2003) describes the distribution of plant functional types (PFTs) over the earth, allowing more than one PFT in a grid cell. For each PFT in a grid cell the fluxes and pools of carbon are simulated based on an average individual of this type. Per PFT, four living biomass pools and three litter pools are distinguished. Two soil carbon pools common to all PFTs are used per grid cell.

Coupling between the atmosphere and the terrestrial biosphere is performed yearly with monthly data. The land surface scheme of the ECHAM3 atmospheric general circulation model (Roeckner et al. 1992) is largely unchanged, but the required input fields are calculated from the simulated vegetation. The vegetation model uses climate parameters from the atmosphere for its calculations, the main parameters are temperature, soil moisture content and radiation. The land surface parameters for the feedback to the atmosphere include parameters influencing both the radiative (albedo, tree fraction) and the turbulent fluxes (vegetation fraction, roughness length). A description of the coupling with these parameters is given below. By varying these parameters between active coupling and prescribed values, the magnitude of their effects on the simulated climate change can be determined.

Due to the yearly coupling between atmosphere and land surface, a lag of 1 year emerges between the changes in climate and the land surface response to these. However, because the time scales of interest for the land surface processes are much longer for this study, this will not have a substantial influence on the land surface effects

2.1 Land surface parametrization

The albedo of the land surface has a large impact on the energy balance. It is determined by the type of vegetation cover, the visibility and colour of the bare soil and the presence and smoothness of a snow cover. For the calculation of the background albedo (albedo of the surface without snow cover), the grid cell area is divided over several sub-grid parts: a part that is covered by leaf-covered vegetation, a part that is covered by leafless vegetation and a part that is covered by bare soil. The grid-cell albedo is a weighted average of the albedo values assigned to these compartments:

$$\alpha = c_{\mathrm{v}}\alpha_{\mathrm{veg,l}} + (c_{\mathrm{v,max}} - c_{\mathrm{v}})\alpha_{\mathrm{veg,nl}} + (1 - c_{\mathrm{v,max}})\alpha_{\mathrm{soil}}. \quad (1)$$

In this equation, c_{v} is the leaf-covered vegetation fraction, $c_{\mathrm{v,max}}$ is the maximum vegetation fraction and $\alpha_{\mathrm{veg,l}}$, $\alpha_{\mathrm{veg,nl}}$ and α_{soil} are the albedoes for leaf-covered vegetation, leafless vegetation and soil. The leaf-covered vegetation albedo is constructed from the albedoes of the plant functional types. Each plant functional type was assigned an albedo value (see Table 1), and the values are averaged according to the fraction of (leaf-covered) vegetated area they cover:

$$\alpha_{\mathrm{veg,l}} = \frac{\sum_i (\varphi_i c_{\mathrm{v},i}\alpha_i)}{\sum_i (\varphi_i c_{\mathrm{v},i})}, \quad (2)$$

in which φ_i is the phenology state (between 0 and 1, see Sitch et al. 2003), $c_{\mathrm{v},i}$ is the maximum cover fraction and α_i is the albedo of the plant functional type i. The albedo values α_i in Table 1 were derived from Claussen (1994),

Table 1 Albedo (α) and roughness length (z_0) assigned to the plant functional types

PFT	Description	α_i	$z_{0,i}$
1	Tropical broad-leaved evergreen	0.12	2.00
2	Tropical broad-leaved raingreen	0.12	2.00
3	Temperate needle-leaved evergreen	0.13	1.00
4	Temperate broad-leaved evergreen	0.13	1.00
5	Temperate broad-leaved summergreen	0.16	1.00
6	Boreal needle-leaved evergreen	0.13	1.00
7	Boreal needle-leaved summergreen	0.16	1.00
8	Boreal broad-leaved summergreen	0.16	1.00
9	Temperate herbaceous	0.20	0.03
10	Tropical herbaceous	0.20	0.03

with albedoes for 17 biomes, and Claussen et al. (1994), with albedoes for 13 simple surface types. The values are in agreement with albedo values given in Wilson and Henderson-Sellers (1985), Hagemann et al. (1999) and Milly and Shmakin (2002). A constant albedo for non-leaf-covered area of all plant functional types $\alpha_{\mathrm{veg,nl}} = 0.16$ was used. The bare soil albedo is dependent on the soil colour (which is given as input) and on the soil water content (Wilson and Henderson-Sellers 1985). It is calculated as

$$\alpha_{\mathrm{soil}} = w\alpha_{j,\mathrm{wet}} + (1-w)\alpha_{j,\mathrm{dry}}, \tag{3}$$

in which w is the relative moisture content of the soil, and $\alpha_{j,\mathrm{wet}}$ and $\alpha_{j,\mathrm{dry}}$ are the albedoes for wet and dry soil of soil colour j. The soil colour map that is used as input, as well as the albedo values for dark, medium and light soil, were derived from Wilson and Henderson-Sellers (1985). In ECHAM3, the total surface albedo is calculated from background albedo and snow cover albedo. For the calculation of the snow cover albedo, the tree fraction (or forest fraction) from LPJ is used. It is calculated as the sum of maximum cover fractions $c_{\mathrm{v},i}$ for all tree PFTs. Snow cover albedo for forested areas lies between 0.3 and 0.4, snow cover albedo for unforested areas lies between 0.4 and 0.8, dependent on surface temperature (Kukla and Robinson 1980; DKRZ 1993).

The surface roughness is defined as the height above the ground that is obtained when the logarithmic wind profile from well above the canopy is extrapolated to the point where the wind speed would have been 0, thereby ignoring changes in the profile next to the surface. It is used in ECHAM3 to calculate drag coefficients for the fluxes for water, energy and momentum (DKRZ 1993). Surface roughness is constructed from the orography roughness and the vegetation roughness length (Claussen et al. 1994):

$$z_0 = \sqrt{z_{0,\mathrm{oro}}^2 + z_{0,\mathrm{veg}}^2}. \tag{4}$$

The vegetation roughness is determined by the amount of vegetation and the type of vegetation. The roughness lengths per plant functional type $z_{0,i}$ were derived from Claussen (1994) and Claussen et al. (1994), and are shown in Table 1. The vegetation roughness length is calculated from the averaged drag coefficients (Claussen 1991; Claussen et al. 1994), which uses a blending height z_{b}:

$$\frac{1}{\ln^2\left(\frac{z_{\mathrm{b}}}{z_{0,\mathrm{veg}}}\right)} = \sum_i \frac{c_{\mathrm{v},i}}{\ln^2\left(\frac{z_{\mathrm{b}}}{z_{0,i}}\right)} + \frac{1-c_{\mathrm{v,max}}}{\ln^2\left(\frac{z_{\mathrm{b}}}{z_{0,\mathrm{soil}}}\right)}. \tag{5}$$

The last part of the equation calculates the contribution of bare soil to the vegetation roughness length. Soil roughness $z_{0,\mathrm{soil}} = 0.005$ m and the blending height $z_{\mathrm{b}} = 100$ m, as taken from Claussen et al. (1994). The orography roughness $z_{0,\mathrm{oro}}$ (Eq. 4) is given as input, and was derived from the original ECHAM3 roughness length field.

The amount of vegetation influences evaporation. ECHAM3 uses the vegetation fraction (the fraction of a grid cell covered with vegetation) to calculate evaporation (DKRZ 1993). This fraction is the sum of all individual PFT covers, corrected with the phenology state of each PFT. Vegetation fraction, as well as surface background albedo, features a seasonal cycle, based on the phenological changes of the vegetation.

2.2 Experiments

An experiment was carried out in which insolation was prescribed for the time period 128–113 ky BP (15,000 years) according to Berger (1978). A 1,000-year spinup run was performed for this experiment, starting from present-day conditions and running with an insolation forcing according to 129–128 ky BP. In addition, a control run of 10,000 years with present-day insolation was carried out. Besides these two long runs, a set of experiments for the same period were performed with an accelerated insolation forcing, in order to study the influence of the land surface in detail. These experiments were performed with either an interactive or a prescribed (present-day) land surface, as well as two 'partially interactive' experiments: one in which the land surface was only interactive for tree fraction, and one in which the land surface was interactively coupled except for the land surface background albedo. In this set of accelerated experiments, insolation changes were accelerated with a factor 8, so that the model was integrated for 1,875 years. Two additional control runs were performed with present-day insolation (one with a completely interactive land surface, one with a completely prescribed land surface), with the same parameter settings as in the accelerated experiments. An interactive land surface is denoted with (+), fixed land surface parameters with (–) for the experiments, accelerated experiments (as well as the control runs to these experiments) are preceded by 'A'. The experiments are summarized in Table 2.

Coupling between the atmosphere and the other components was done with a periodically-synchronous coupling technique (Sausen and Voss 1996). In contrast to the original version, where the fluxes were kept constant during the period without interactive calculation of the atmospheric GCM, an energy balance model is applied here to get an appropriate feedback on sea surface temperature and sea ice. Details are given in Mikolajewicz et al. (2007). For the accelerated experiments, the maximum length of the asynchronous period and the cutoff value for the heat flux anomaly, which determine the length

Table 2 Overview of the experiments

$CTRL^+$	Control run with present-day insolation (10,000 years)
INS^+	Insolation experiment (15,000 years)
$ACTRL^+$	Control run with present-day insolation, with interactive land surface
$ACTRL^-$	Control run with present-day insolation, with prescribed (present-day) land surface
$AINS^+$	Insolation experiment, with interactive land surface (accelerated)
$AINS^-$	Insolation experiment, with prescribed land surface (accelerated)
$AINS^+A^-$	Insolation experiment, with interactive land surface, but with prescribed background albedo (accelerated)
$AINS^-F^+$	Insolation experiment, with prescribed land surface, but with interactive tree fraction (accelerated)

of the asynchronous coupling period (Mikolajewicz et al. 2007), were reduced compared to the unaccelerated experiments. This does not affect the average climate of the model, but it might have an effect on the variability.

For the experiments with a prescribed land surface, the vegetation model was still included for analysis of the vegetation changes, but changes in the vegetation were not allowed to affect the atmosphere model. The atmosphere and vegetation model run on a T21 grid (roughly $5.6° \times 5.6°$), the ocean and ocean biogeochemistry on an Arakawa E-grid (effectively $4.0° \times 4.0°$).

3 Results

3.1 Land surface parametrization

The climatological land surface parameters from the control run ($CTRL^+$) will be compared with the original ECHAM3 input (as used for the $ACTRL^-$ and $AINS^-$ experiments). The ECHAM3 input fields were mainly derived from satellite measurements, depicting the situation as influenced by man. The vegetation and land surface as modelled from the dynamic vegetation model do not take human influence (e.g. deforestation, land use) into account. It describes a 'present-potential' vegetation.

The simulated vegetation pattern for present-potential conditions was described in Schurgers et al. (2006), and shows in general a good agreement with what is considered as present-potential vegetation. The Amazon region is dominated by Savanna due to underestimated precipitation rates in the atmosphere model, and the high latitudes in Europe and Asia are too cold in the control run compared to observations, resulting in an anomalous southward shift of the vegetation zones.

Vegetation cover, as well as surface background albedo is simulated with an annual cycle. Figure 1 compares the yearly average surface conditions from the control run (vegetation and tree cover fraction and background albedo) with the yearly values of the original ECHAM3 parametrization. For both vegetation and tree cover fraction, model results differ substantially from the original input. For the vegetation cover in Fig. 1b, it should be noted that the original ECHAM3 model does not consider a yearly cycle for the vegetation cover, whereas the newly coupled version does, and that vegetation cover is corrected with a dependence on soil moisture content in the ECHAM3 parametrization, which was taken into account for Fig. 1a. The simulated vegetation cover shown here is the maximum cover that is obtained throughout the year. Large differences occur due to the presence of human influence in the ECHAM3 parametrization, which was not simulated with the model.

Although vegetation and tree cover differ substantially, background albedo changes only moderately for most regions with the newly introduced parametrization (Fig. 1c). Large differences occur in the highest latitudes, where the original parametrization shows high albedo values, whereas the modelled land surface shows particularly low albedoes, due to the presence of dark soils. The original satellite-derived parametrization could be biased here due to snow cover influence, which should not be taken into account in the background albedo, and the modelled values could be too low, because they are based on bare soils, whereas vegetation exists here, which is not simulated by the model. For the rest of the earth, the albedoes match quite well. Over tropical forest, the modelled albedoes are slightly lower than from the original parametrization, the temperate and boreal regions show good agreement, as well as the desert regions in North Africa and Southern Asia.

The control runs with and without interactive land surface vary only slightly in climate. Global surface air temperature is 286.2 K for both control runs ($ACTRL^-$ and $ACTRL^+$), with a standard deviation of 0.27 K for the experiment with fixed land surface ($ACTRL^-$) and a standard deviation of 0.18 K for the experiment with interactive land surface ($ACTRL^+$). Local changes in annual temperature between the control run with interactive land surface ($ACTRL^+$) and the control run with fixed land surface ($ACTRL^-$) reach from –2 K for Central Asia and Northwest Africa to +3 K for Arabia, mainly caused by changes in the background albedo (Fig. 1c). Relatively

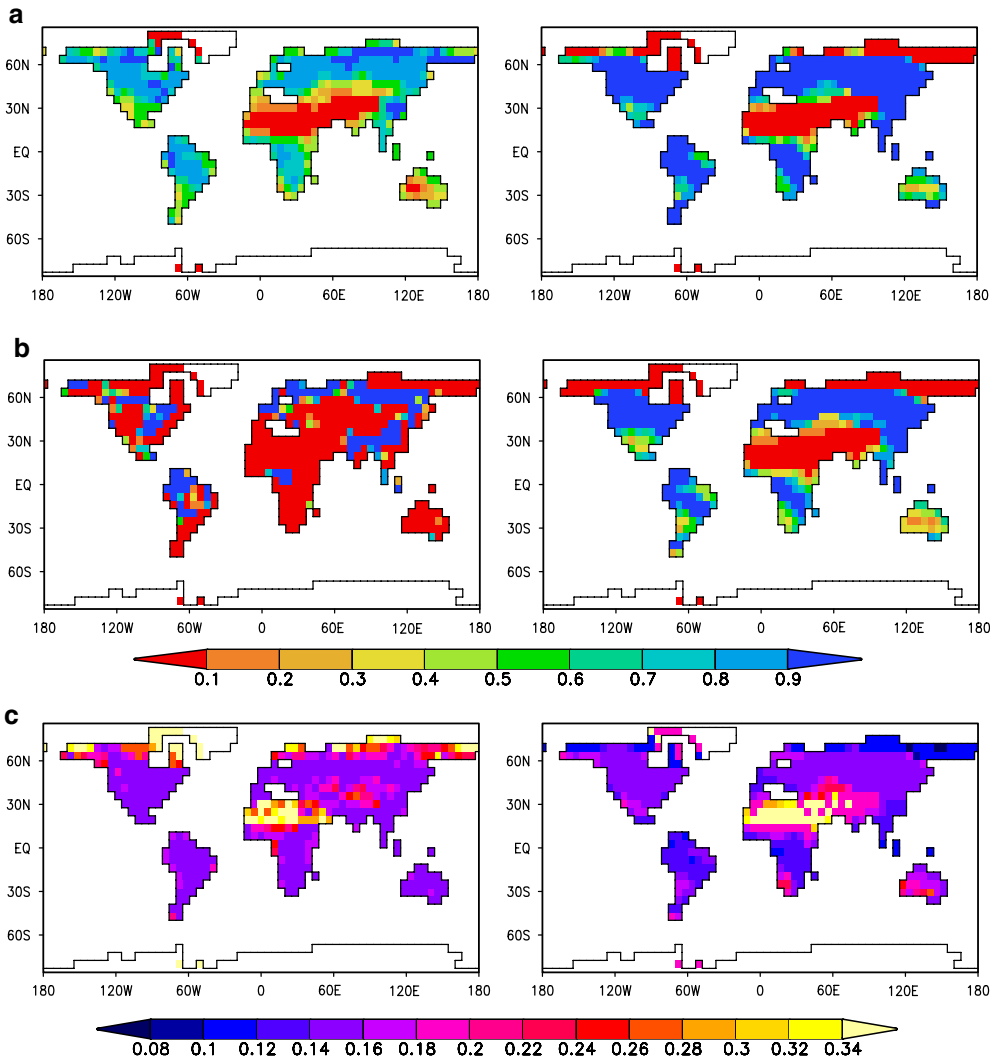

Fig. 1 Land surface parameters in ECHAM3 (*left*) and average of the control run ($CTRL^+$) with the new parametrization (*right*). **a** Vegetation cover (in ECHAM3 corrected for soil wetness, for the $CTRL^+$ experiment average growing season vegetation cover is shown), **b** tree cover, **c** surface background albedo (for the $CTRL^+$ experiment the yearly average is shown)

large differences are simulated near Antarctica, however these differences are smaller than two standard deviations of the control run.

The effect of the newly introduced land surface coupling on precipitation is relatively small. The main exception is the monsoon over India and Southeast Asia, which expands slightly northward, thereby extending the land surface area that is affected. A slight decrease in precipitation is simulated over Northern Africa.

3.2 Climate change

The total annual amount of incoming solar radiation at the top of the atmosphere is only slightly higher under Eemian conditions than under present-day conditions, with a small change over the period from 128 to 113 ky BP (0.11–0.13 PW more than present, Fig. 2a). The large changes that occur in the climate over this period are caused by changes in the spatial and temporal distribution of the radiation (Fig. 2b, c). In the following we discuss anomalies of selected time slices as well as time series from the insolation experiments to the respective control run.

For the early Eemian, the coupled experiment (INS^+), as well as the accelerated coupled experiment ($AINS^+$), simulate higher (more than 1 K) annual mean surface temperatures on the northern hemisphere. From approximately 125 ky BP till 115 ky BP a gradual cooling of the northern hemisphere earth surface of nearly 1.5 K is simulated (Fig. 3). The southern hemisphere shows a very moderate warming trend during the first 5,000 years of the simulation. During the last 5,000 years of the insolation experiments a moderate cooling trend is obvious. The variability here is much higher than in the northern hemisphere for both the insolation runs and the control run (standard deviations for the control run $CTRL^+$ are 0.15 K for the northern hemisphere and 0.42 K for the southern hemisphere). This high century scale variability is caused by variations in the convection in the Weddell Sea and Ross

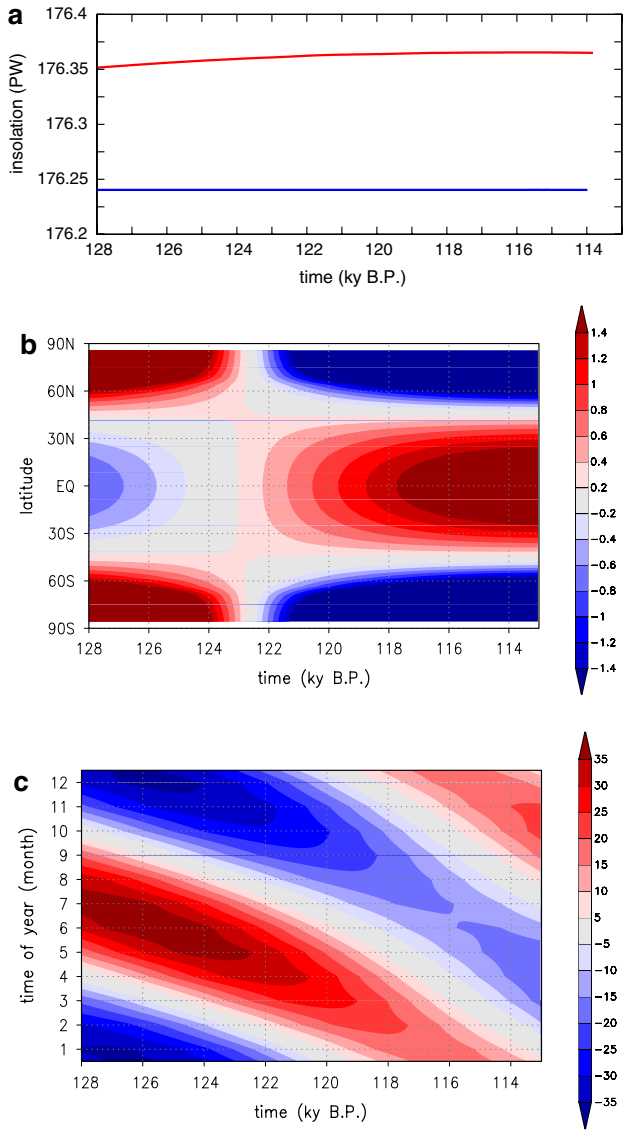

Fig. 2 Total incoming solar radiation at the top of the atmosphere over the period 128–113 ky BP. **a** Annual mean total incoming radiation (in *red*, with present-day value in *blue*). **b** Anomalies of the latitudinal distribution of the annual mean solar radiation (W m^{-2}) compared to present-day. **c** Time evolution of anomalies of the seasonal cycle of incoming solar radiation (W m^{-2}) compared to present-day

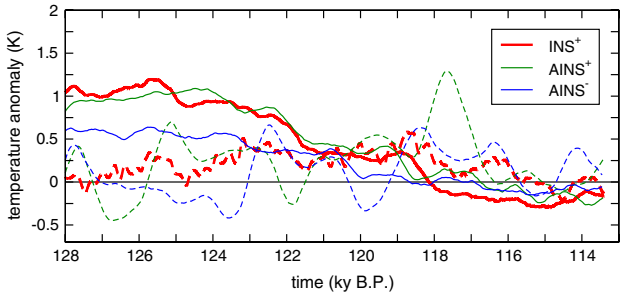

Fig. 3 Average surface air temperature anomalies (K) for the fully coupled insolation experiment (INS^+), and the accelerated insolation experiments with interactive land surface ($AINS^+$) and with fixed land surface ($AINS^-$) for the northern (*full line*) and southern (*dashed line*) hemisphere to the climate of the respective control runs ($CTRL^+$, $ACTRL^+$ and $ACTRL^-$). Shown are 0.8 ky running means

Sea (see Mikolajewicz et al. 2007). For the accelerated experiments, the variability seems to be higher in the running means, especially in the southern hemisphere, which is a result of averaging over fewer model years due to the acceleration.

The higher surface temperatures shown in the northern hemisphere for the first half of the experiment are mainly taking place during summer, in consistence with the insolation forcing (Fig. 4a). Annual mean surface temperature anomalies in the insolation experiment INS^+ (compared to the control run $CTRL^+$) are larger over the land surface than over the ocean, with a strong positive anomaly for the entire northern hemisphere. The northern hemisphere monsoon regions (North Africa, Southeast Asia) are remarkable exceptions, with a cooling for the period 127–125 ky BP of up to 5 K during summer (Fig. 4a) and up to 4 K in the annual mean (Fig. 5a). The monsoon circulation differs here considerably from the control run due to an enhancement of rising air over the land surface and an enhancement of sinking air over the ocean compared to present, resulting in a huge precipitation increase for Northwest Africa (Fig. 5b). The negative temperature anomaly and positive precipitation anomaly for the beginning of the Eemian compared to the control run are closely related: increased cloud cover (Fig. 4b) decreases the incoming radiation and increased evaporation causes an additional latent heat loss.

To isolate the transient insolation signal, the empirical orthogonal functions (EOFs, Preisendorfer 1988) from the INS^+ experiment were calculated for surface temperature and precipitation. Hundred year mean anomalies to the control run $CTRL^+$ served as input for the analysis. The first EOFs of temperature and precipitation explain each more than 40% of the total variance in the data set.

The first principal component time series (Fig. 6a) of both temperature and precipitation show a clear insolation signal, following the decrease of incoming radiation in the northern hemisphere mainly caused by changes in the earth's precession. The matching EOF pattern for surface temperatures shows the northern hemisphere warming with maximal amplitude close to the Arctic ocean and the strong cooling in the monsoon areas of Northwest Africa and Southeast Asia. The first EOF of precipitation describes the dipole pattern over the tropical North Atlantic with decrease of precipitation in the west and enhanced precipitation over the Western Sahara. The second EOF of precipitation (explaining 8.3% of the total variance) largely describes the non-linearity in the precipitation response. Over the Sahara it slightly amplifies the precipitation dur-

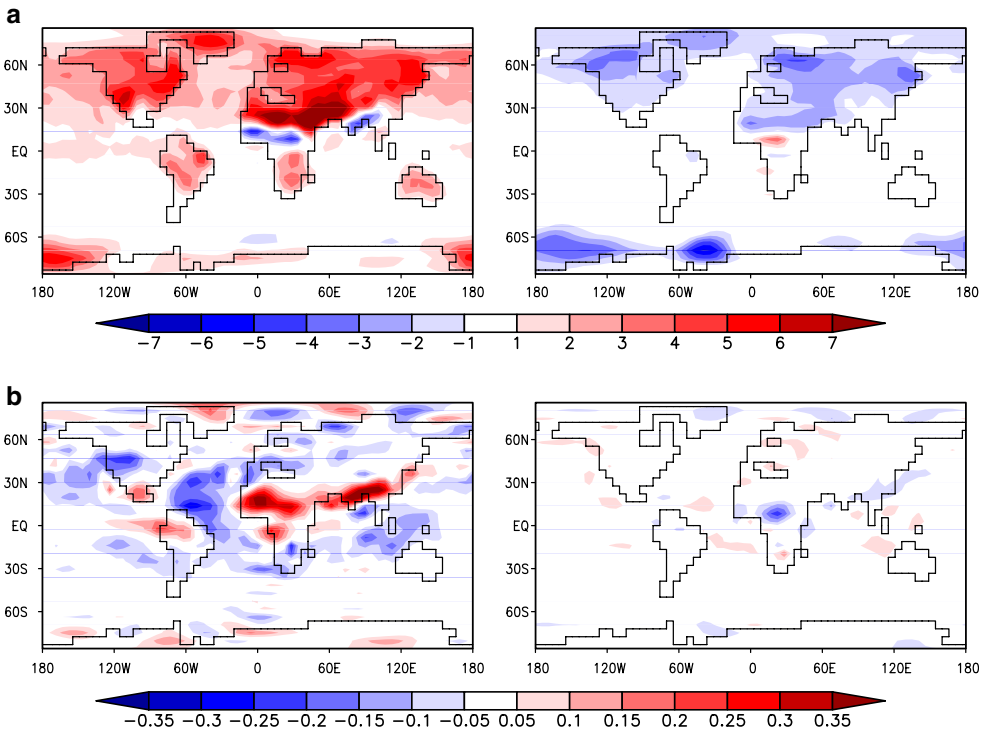

Fig. 4 **a** Surface air temperature anomaly (K) and **b** cloud cover anomaly (–) for summer months (JJA) of 127–125 ky BP (*left*) and 116–114 ky BP (*right*) of the coupled experiments INS^+ relative to the climate of the control run $CTRL^+$

ing the early Eemian, and it strongly reduces the effect of the first EOF around 121 ky BP. This behaviour becomes obvious from the corresponding principal component time series. The other EOFs capture only natural variability of the model, and do not show any insolation signal.

For 116–114 ky BP, the amplitude of the temperature anomalies (relative to the control run) are smaller (Fig. 4a). During summer, lower temperatures compared to the control run were simulated over the northern hemisphere land surface up to 4 K, with slightly higher temperatures and a slightly higher cloud cover (Fig. 4b) over the Sahel zone, which is the opposite effect of that discussed for 127–125 ky BP.

The CO_2 concentration increases during the coupled experiment INS^+, from around 270 ppm for the beginning (128 ky BP) to around 290 ppm around 116 ky BP. This increase is mainly related to a decrease of terrestrial carbon storage (Schurgers et al. 2006). For the accelerated experiments, the increase in CO_2 concentration is smaller, and the changes are delayed compared to the unaccelerated experiment. However, the carbon storage in the accelerated experiments cannot be interpreted directly, as the acceleration caused the insolation changes to happen on time scales comparable to those of deep ocean ventilation.

3.3 Land surface changes

The main features of the changes in climate in the unaccelerated experiment are simulated for the accelerated experiments with and without land surface coupling as well, however the magnitudes of the simulated effects differ. In general, there is much more similarity between the two experiments with interactive land surface (INS^+ and $AINS^+$) than between the two accelerated experiment ($AINS^+$ and $AINS^-$). The latter two experiments show remarkable differences, both in simulated vegetation and in simulated climate (Fig. 5). The temperature pattern as shown for the INS^+ experiment in summer for the period 127–125 ky BP (Fig. 4a) dominates the yearly average for the two accelerated experiments as well, but both the warming in the high latitudes of the northern hemisphere and the cooling in the monsoon area compared to the control run, as described above, are larger for the experiment with interactive land surface ($AINS^+$) than for the experiment with prescribed land surface ($AINS^-$, Fig. 5a). A similar amplification, both of the magnitude and of the spatial extent, can be observed for precipitation (Fig. 5b).

Changes in the surface albedo are considered to be the main cause of these amplifications. Figure 5c shows the albedo changes compared to the respective control runs. For the $AINS^-$ experiment, background albedo was prescribed, so changes in surface albedo are only caused by changes in the snow cover and changes in sea ice cover. Over land, minor changes in surface albedo can be observed for the high latitudes. However, if the changes in vegetation cover are allowed to influence the albedo, as in the interactive experiment ($AINS^+$), large areas with a

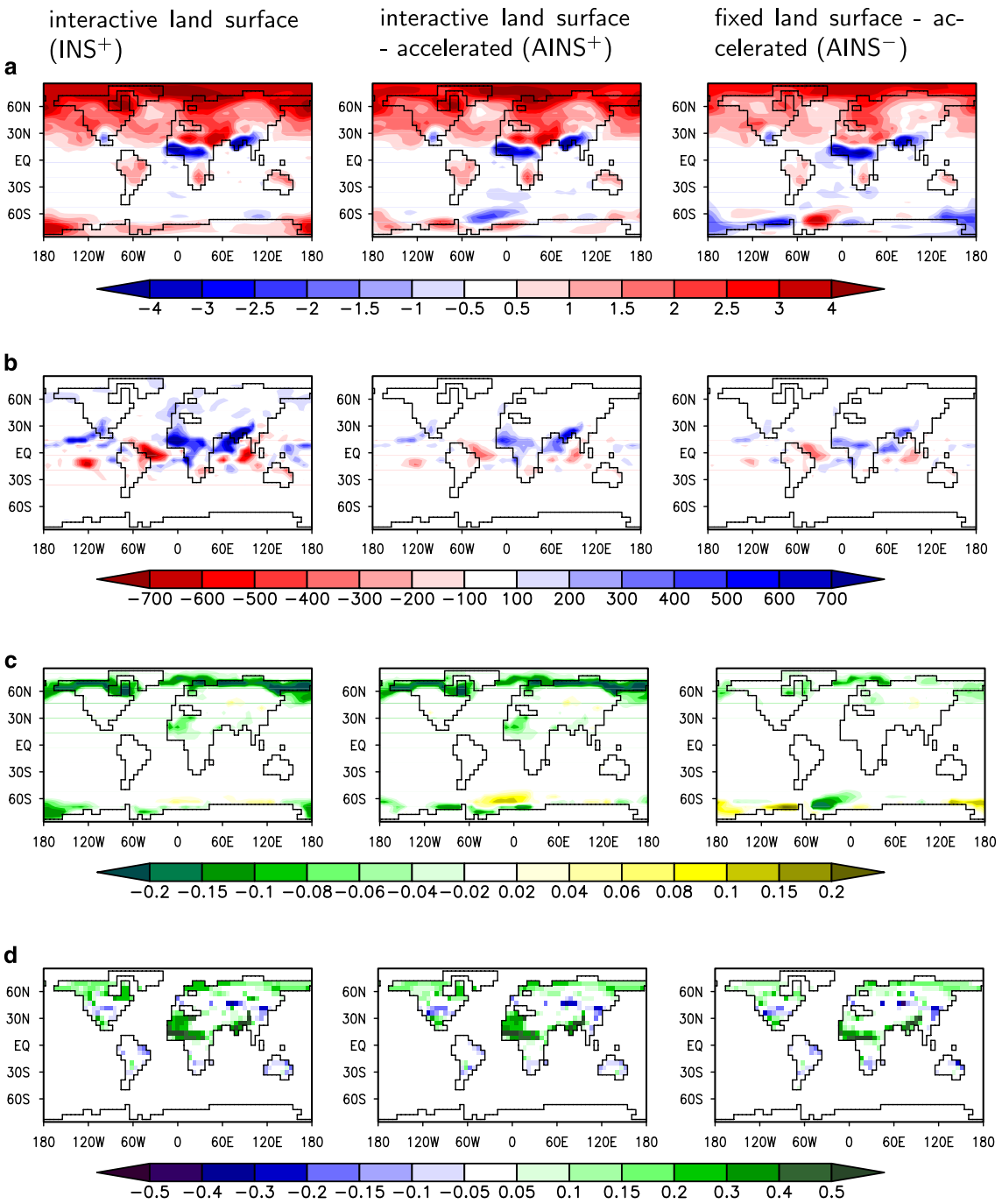

Fig. 5 127–125 ky BP annual anomalies of **a** surface air temperature (K), **b** precipitation (mm year^{-1}), **c** surface albedo (–) and **d** average vegetation cover (–), for the experiment with interactive land surface (INS$^+$–CTRL$^+$, *left*) and the accelerated experiments with interactive land surface (AINS$^+$–ACTRL$^+$, *middle*) and fixed land surface (AINS$^-$–ACTRL$^-$, *right*)

decreased albedo compared to the control run (ACTRL$^+$) can be observed for the high latitudes, as well as for Northwest Africa. These changes are related to changes in the vegetation cover (Fig. 5d), which themselves are often amplified by the coupling as well. Positive feedbacks between vegetation and climate cause this amplification of the changes due to changes in insolation in the high latitudes of the northern hemisphere and in the monsoon areas over North Africa and Southeast Asia.

These local changes in the land albedo, and to a lesser extent changes in the vegetation cover, cause changes in the energy balance of the earth, not only in the areas that are directly subject to these changes, but in other parts of the earth as well, as discussed below.

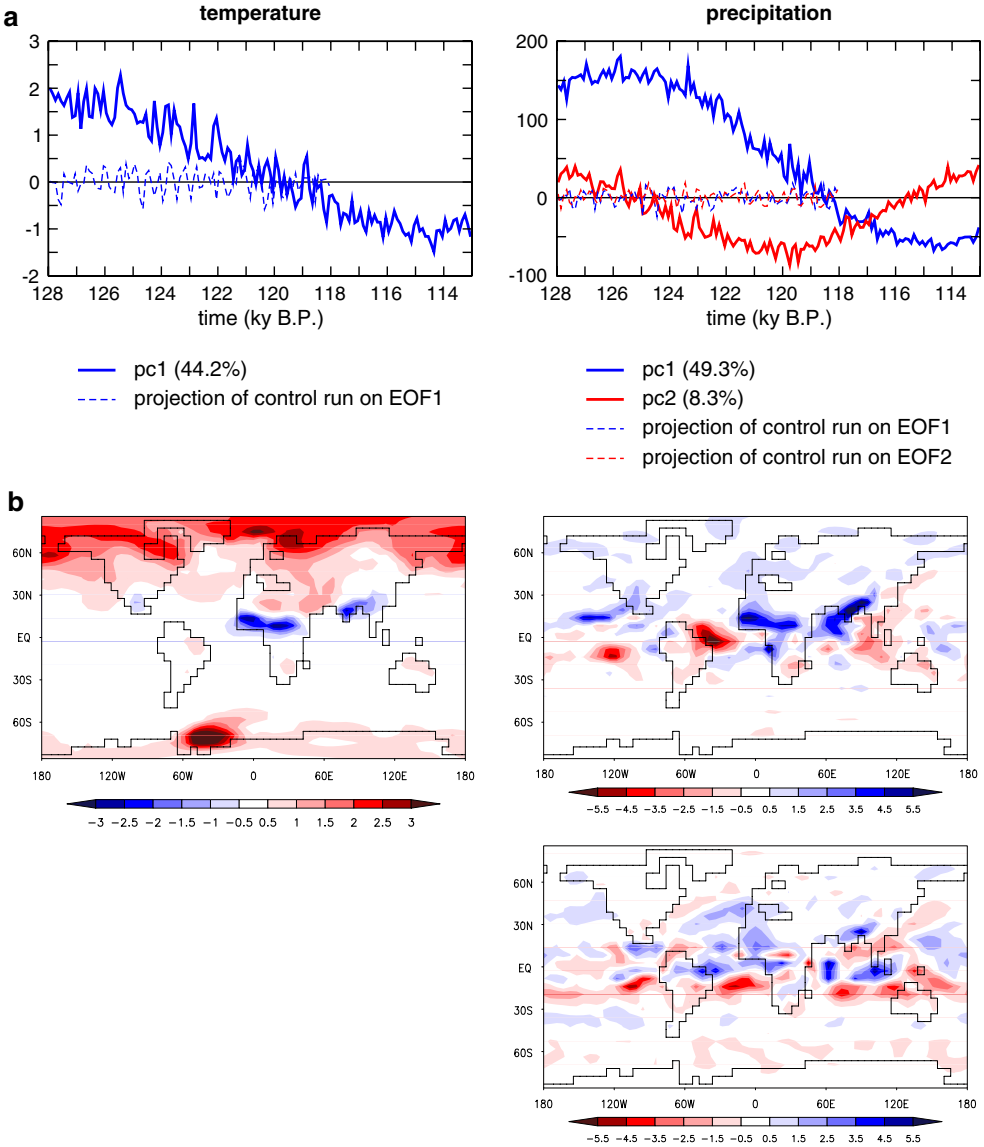

Fig. 6 **a** Prinicpal components for surface temperature (*left*, K) and precipitation (*right*, mm year^{-1}), **b** the corresponding EOF patterns. The analysis was performed with 100-year averages. The climate pattern can be obtained by the multiplication of the value of the principal component time series and the respective EOF pattern, summed over all EOFs

3.3.1 High latitude boreal forest and tundra

Over the high latitudes in the northern hemisphere, boreal forests cover large areas up to the Arctic Ocean in the early Eemian (Fig. 5d), extending further north than the boreal forests in the control simulations. Over the time span of the transient experiment, they show a gradual decrease in cover north of 60°N (Fig. 7a), which can be interpreted as a southward retreat of the treeline for most of the northern hemisphere regions. Until 120 ky BP, temperate forests are present as well in higher latitudes, but they show a substantial southward retreat afterwards. Grasses stay constant or increase slightly for some boreal areas, occupying the area that is abandoned by boreal trees.

For all insolation experiments, the land surface between 60° and 90°N is simulated to be warmer than for the control runs between 128 and 122 ky BP (Fig. 7c), causing these changes in vegetation. For the experiment with fixed land surface (AINS^{-}), a maximum difference between insolation run and control run of 1.5 K is simulated, which is due to an increase in incoming shortwave radiation, and which is only very slightly enhanced by a snowcover-induced albedo decrease (Fig. 7b). This effect is enhanced in the experiments with interactive land surface (INS^{+} and AINS^{+}), because changes in tree fraction (Fig. 7a) and background albedo cause a decrease in surface albedo compared to the control runs (CTRL^{+} and ACTRL^{+}, Fig. 7b). A positive temperature anomaly of more than 3 K was simulated for the early Eemian.

From 118 ky BP onwards, the opposite effect can be observed, with enhanced albedo increase and surface temperature decrease due to land surface changes. Thus vegetation changes at high northern latitudes enhance the simulated climate changes by almost a factor of 2. Two

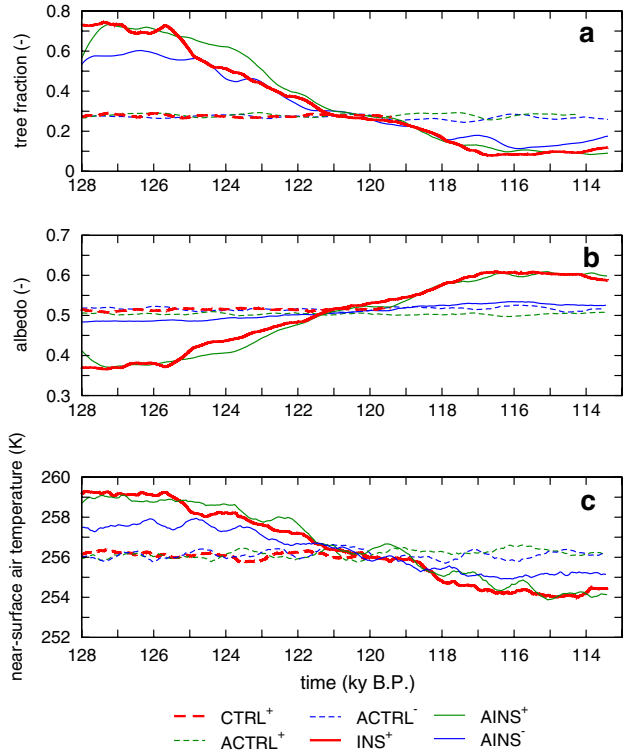

Fig. 7 Annual mean tree fraction (**a**), surface albedo (**b**) and surface air temperature (**c**) for the land surface 60°–90°N (excluding ice sheets). Shown are 0.8 ky running means from the unaccelerated experiments ($CTRL^+$ and INS^+), the control runs ($ACTRL^-$ and $ACTRL^+$) and the accelerated insolation experiments ($AINS^-$ and $AINS^+$). Tree fractions from $ACTRL^-$ and $AINS^-$ are simulated for diagnostical purposes only and are not influencing the surface properties as seen by the atmosphere

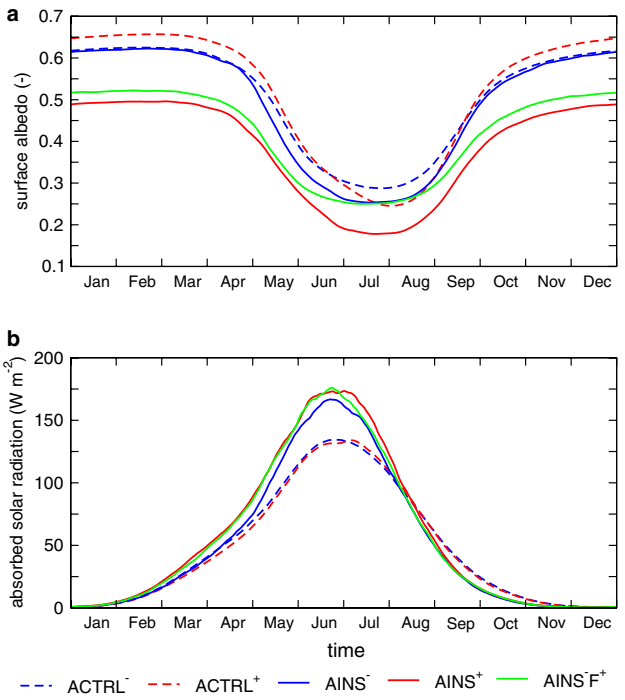

Fig. 8 Seasonal cycle of land surface albedo (**a**) and absorbed shortwave radiation (**b**) by the land surface for the northern hemisphere high latitudes (60°–90°N) for 127–125 ky BP. Shown are 10-day running means

explanations are important for the decrease of surface albedo for the period 128–120 ky BP: (1) the albedo for forest is lower than for grasses, and (2) the albedo for a snow-covered forest is lower than for a snow-covered tundra, due to a more irregular covering of the surface. The additional experiment $AINS^-F^+$, in which background albedo is prescribed according to the present-day situation (Fig. 1b), but tree fraction is used interactively, can help separating the two effects. The surface albedo is calculated from the background albedo and the snow albedo in the atmosphere model, and tree fraction is used to calculate the latter. In the $AINS^-F^+$ experiment, surface albedo changes are caused only by changes in the tree fraction and thus snow albedo. The albedo of vegetation that was not covered by snow was prescribed according to the present-day situation.

The annual cycle of albedo (Fig. 8a) changes substantially between the control runs $ACTRL^-$ and $ACTRL^+$ and the insolation experiments $AINS^-$ and $AINS^+$. The difference between 126 ky BP in the $AINS^-$ experiment and its control run ($ACTRL^-$) is caused solely by changes in the snow cover: in spring snow melt occurs earlier and faster, resulting in a larger snow-free area during summer. This difference is enhanced with the interactive land surface: land surface albedo is both in summer and in winter below the control run values for 126 ky BP in the $AINS^+$ experiment.

The annual cycle (Fig. 8a) for albedo in the $AINS^-F^+$ experiment is similar to the experiment with interactive land surface ($AINS^+$) during winter and spring, and similar to the experiment with fixed land surface ($AINS^-$) during summer. Changes in winter are larger than changes in summer. However, because the incoming shortwave radiation is much higher during summer, the summer albedo changes are in general of more importance. Figure 8b shows that the seasonal cycle of absorbed solar radiation for the INS^-F^+ experiment differs mostly from the $AINS^-$ experiment in spring and early summer. The yearly total absorbed solar radiation for the land surface between 60° and 90°N is 2.58×10^{22} J for the $AINS^-$, 2.85×10^{22} J for the $AINS^+$ and 2.76×10^{22} J for the $AINS^-F^+$ experiment. For the control runs this is much lower: 2.42×10^{22} J for the $ACTRL^-$ experiment, and 2.37×10^{22} J for the $ACTRL^+$ experiment. This sets the increase in absorbed shortwave radiation due to tree fraction induced snow albedo changes to two-thirds of the total yearly increase due to land surface changes, leaving one-third for vegetation albedo changes and possible synergetic effects.

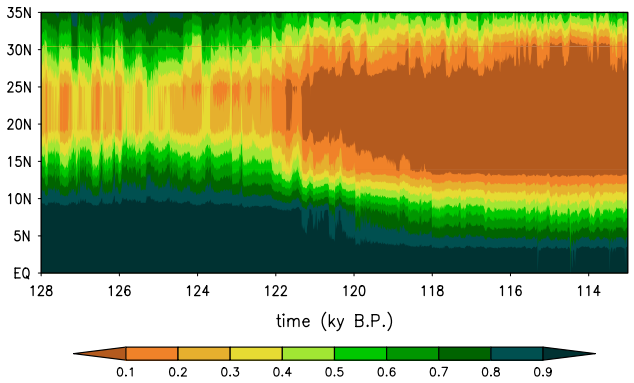

Fig. 9 Time evolution of the zonal mean vegetation cover for Northwest Africa (land surface 10°E–20°W) for the Eemian insolation experiment (INS^+). Shown are 10-year running means

3.3.2 *Sahara desert*

During the first half of the coupled experiment (INS^+), Northwest Africa, including the Sahara region, is covered with vegetation (Fig. 9). Major changes in the vegetation pattern occur here during the course of the experiment: The cover of evergreen trees, both tropical and temperate, present in the area between 5° and 15°N at the beginning, reduce, as well as the cover of herbaceous plants. Between 15° and 30°N, the cover of herbaceous plants reduces clearly during the experiment, and evergreen trees reduce slightly as well. Around 122 ky BP an almost abrupt transition of the Sahara vegetation between 15° and 30°N takes place towards drier conditions with less vegetation. This retreat of the vegetation causes the Sahara region to become a desert (Fig. 9).

Enhanced vegetation cover accompanied by an increase in precipitation (relative to the respective control runs), is simulated for the period 128–120 ky BP in all insolation experiments. The diagnostic simulation of vegetation for the uncoupled transient run ($AINS^-$) shows a clear increase of both vegetation and precipitation compared to all control runs ($CTRL^+$, $ACTRL^-$ and $ACTRL^+$, Fig. 10). Changes in the insolation due to changes in the earth's orbit cause a heating of the land surface in the subtropical and temperate regions in summer compared to present, and thereby an increased temperature gradient between the large land masses and the ocean, thereby enhancing the atmospheric moisture transport of the monsoons. The positive feedbacks between presence of vegetation, land surface albedo and precipitation cause an obvious amplification of this effect by approximately a factor of 3 for the early Eemian in the coupled transient runs (INS^+ and $AINS^+$). A similar amplification was simulated for India, although the magnitude is smaller due to smaller differences between vegetation and soil albedo.

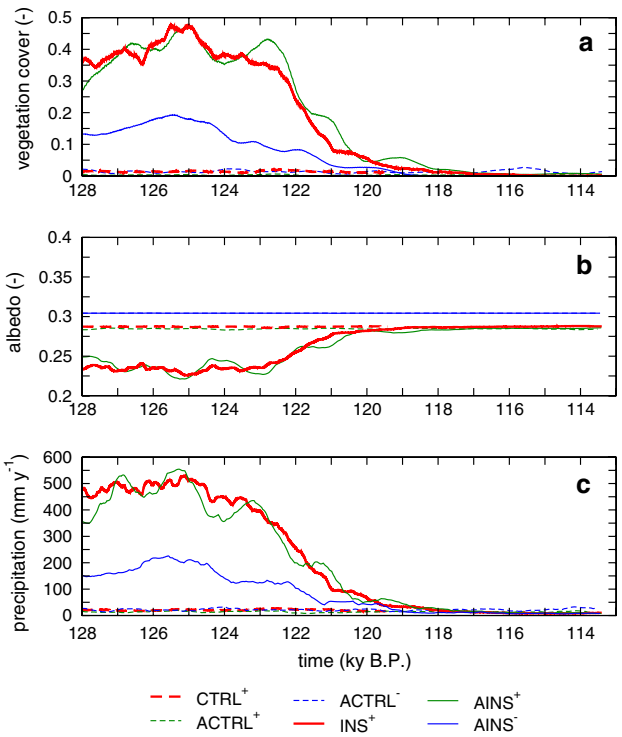

Fig. 10 Annual mean vegetation cover (**a**), surface albedo (**b**) and precipitation(**c**) for the Sahara region (10°E–20°W, 10°–30°N). Shown are 0.8 ky running means from the unaccelerated experiments ($CTRL^+$ and INS^+), the control runs ($ACTRL^-$ and $ACTRL^+$) and the accelerated insolation experiments ($AINS^-$ and $AINS^+$). Vegetation covers from $ACTRL^-$ and $AINS^-$ are simulated for diagnostical purposes only and are not influencing the surface properties as seen by the atmosphere

The patterns of winds at 850 hPa and vertically integrated atmospheric moisture content of the atmosphere for the summer months for 127–125 ky BP are shown in Fig. 11 for the monsoon area over North Africa and India. There are clear differences between the experiment with prescribed ($AINS^-$) and the experiment with interactive ($AINS^+$) land surface: Over West Africa the southwesterly winds coming from the Atlantic Ocean are stronger in case of an interactive land surface, thereby advecting more moisture into the Western Sahara region. The continental winds coming from the north are clearly weaker. This results in an increase in atmospheric moisture content, especially over large parts of Western Africa.

The positive feedback between vegetation and precipitation is supposed to be mainly driven by changes in albedo. Charney (1975) presented a mechanism which links a decrease in albedo to an increase in rising air and in convection and thereby an increase in precipitation, related to an increase of energy near the surface of the atmosphere from enhanced sensible and latent heat loss of the surface. According to Eltahir (1996), Eltahir and Gong (1996) and Braconnot et al. (1999) this energy increase drives the in-

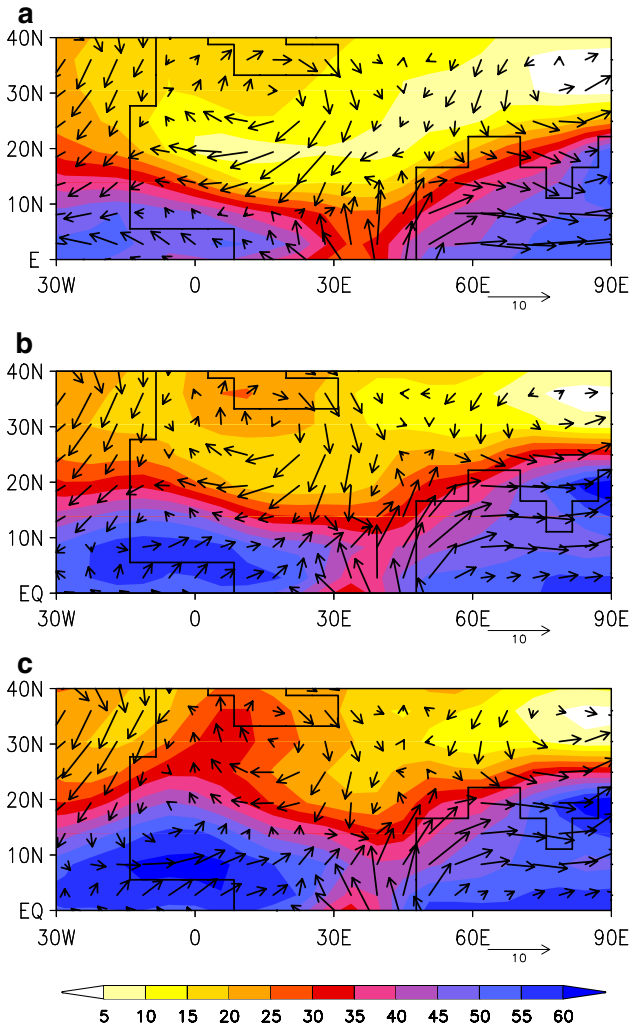

Fig. 11 Average summer (JJA) winds at pressure level 850 hPa (*arrows*, indicated arrow is 10 m s^{-1}) and average summer integrated atmospheric moisture content (kg m^{-2}, *colours*) for the uncoupled control run ($ACTRL^{-}$) (**a**) and for 127–125 ky BP (**b**) with fixed land surface ($AINS^{-}$) and with interactive land surface ($AINS^{+}$) (**c**). Shown are the African and Indian monsoon regions

creased moisture transport from the ocean into Northern Africa, which drives the precipitation increase. It is hard to distinguish between them, because both effects are in principle resulting in an enhancement of the monsoon circulation. Both effects are caused by the change in albedo, as shown in Fig. 10b, and result in the modified circulation pattern in Fig. 11. Besides this albedo change, the hydrological cycle is further amplified by a recycling of water: the presence of vegetation enhances evaporation and thereby precipitation again. In Northwest Africa, more than half of the precipitation between 15° and 25°N that occurs during the summer monsoon (Fig. 12e) is evaporated again.

To verify the importance of the land surface albedo, the additional experiment $AINS^{+}A^{-}$ was performed. In this experiment, background albedo was prescribed, but all other land surface parameters were allowed to vary with the simulated vegetation changes.

In Fig. 12, the $AINS^{+}A^{-}$ experiment is compared with the $AINS^{+}$ and $AINS^{-}$ experiments. The intensification of the monsoon for the period around 126 ky BP compared to present is shown clearly, both the uncoupled and the coupled experiments show a northward expansion of the precipitation pattern in summer, and in general higher precipitation rates. The simulated patterns in the $AINS^{+}A^{-}$ experiment are basically the same as in the experiment without interactive land surface ($AINS^{-}$, compare Fig. 12c, d, e), whereas the precipitation in the experiment with a fully interactive land surface ($AINS^{+}$) expands much further northward. These results confirm that background albedo, the only parameter that differs between these experiments, is the main feedback factor for the enhancement of Sahara rainfall due to dynamic vegetation changes during the early Eemian.

3.4 Effects of land surface changes on the global energy balance

Figure 13 shows an overview of the global energy balance in the control run, and the anomalies for 126 and 115 ky BP. As was discussed above, the globally and annually integrated incoming radiation changes only slightly between control run, 126 and 115 ky BP, with the anomalies for 126 and 115 ky BP being quite similar. However, the changes in the spatial and temporal distribution cause larger anomalies for other components of the energy balance. For most budgets the anomalies in the insolation experiment differ statistically significantly from the control run (Fig. 13). These differences are up to one order of magnitude larger than the changes in annually integrated global incoming radiation, which indicates that these spatial and temporal changes are of great importance.

For 126 ky BP, total cloud cover is higher, especially in the monsoon areas of the northern hemisphere (Fig. 4b), causing the solar radiation reflected and absorbed by the atmosphere to increase, and the amount of solar radiation reaching the earth surface to decrease. This effect is stronger over land than over the oceans. Due to lower albedoes of the ocean (caused by a decrease of sea ice cover) and the land surface (caused by the 'greening' of the Sahara region and the extension of boreal forests in high latitudes), the amount of solar radiation reflected by the surface decreases even more than the decrease of incoming shortwave radiation, especially for the land surface (–1.1 W m^{-2}). The negative albedo anomalies for 126 ky BP cause a slight increase of absorbed shortwave radiation at the surface for land and ocean, despite the smaller

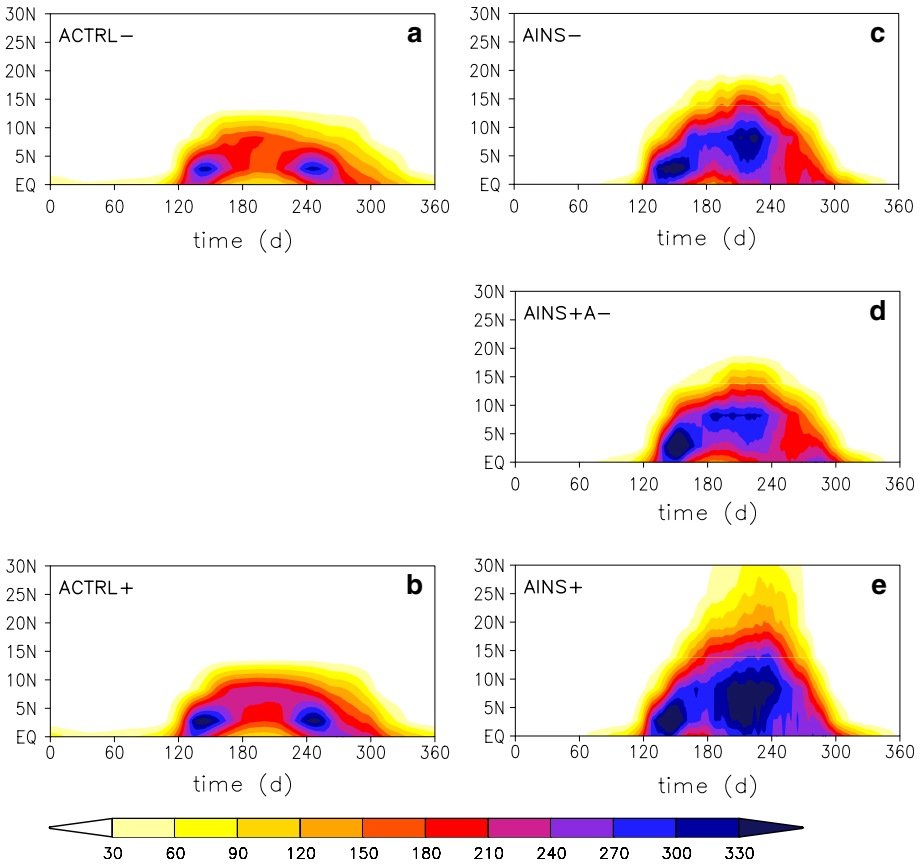

Fig. 12 Zonally averaged annual cycle of precipitation on land (mm month^{-1}) for the Western Sahara region (10°E–20°W), for the control experiments (*left*) and for the accelerated insolation experiments (*right*) for 127–125 ky BP. The *top panels* show the experiments with fixed land surface, the *bottom panels* show the experiments with fully interactive land surface, and the *middle panel* shows the experiment with interactive land surface but fixed background albedo

incoming flux. For 126 ky BP, the outgoing shortwave radiation at the top of the atmosphere shows a clear positive anomaly in the monsoon area over Southeast Asia, Northern Africa and the Arabian Sea compared to present, where cloud cover increases (see Fig. 4b), and a slight negative anomaly compared to present in the high latitudes of the northern hemisphere, where the effective albedo decreases due to land surface changes.

The high cloud cover for 126 ky BP causes as well big changes in the longwave radiation at the surface: downward longwave radiation increases by 2.5 W m^{-2} over land and by 2.0 W m^{-2} over the ocean, which is partially counterbalanced by an increase of outgoing longwave radiation due to increased temperatures of the surface (+1.4 W m^{-2} over land, +1.7 W m^{-2} over the ocean). Because cloud cover changes are much smaller for 115 ky BP, the anomalies in the energy fluxes mentioned above are all much smaller. Due to a slight cooling for 115 ky BP (Fig. 4a), the incoming and outgoing thermal radiation at the surface decrease slightly for 115 ky BP, with in general stronger effects for the land than for the ocean, caused by larger temperature anomalies.

For 126 ky BP, the fluxes of latent and sensible heat show considerable changes compared to the control run, mainly for the land surface. Although the absolute changes are comparable to those of other fluxes, the relative change of especially latent heat over the land surface is very large. Due to higher temperatures, and an increase of vegetation cover and soil wetness mainly in the Sahara region, evaporation increases drastically, causing an increase in latent heat loss for the land surface (+1.6 W m^{-2} or +13.8%) compared to the control run. This is only to a small part counterbalanced by a decrease in sensible heat loss (–0.2 W m^{-2}). Latent heat loss is the main factor compensating the imbalance in longwave radiation at the surface. The main changes in latent as well as sensible heat loss take place in the tropics (Fig. 13), with a dominant role for North Africa.

The effects on the incoming radiation at the surface are in general much lower for the experiment without land surface coupling (AINS$^-$) than for the experiment with land surface coupling (AINS$^+$). Land surface changes are a significant amplifier of the energy balance effects due to changes in insolation for this time period, even on a global scale.

4 Conclusions and discussion

A parametrization for land surface properties was presented, which describes the changes in land surface properties in dependence of the simulated vegetation. Transient

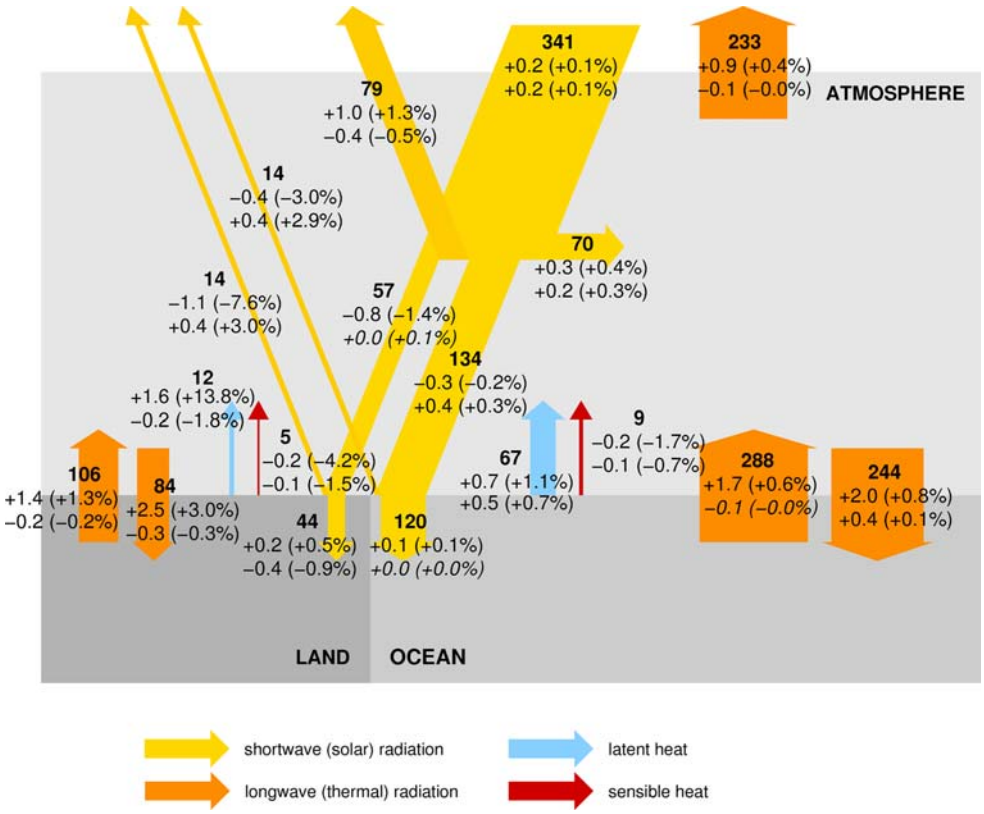

Fig. 13 Overview of the global energy balance for the control run CTRL^{+} and anomalies for 127–125 ky BP (*upper value*) and 116–114 ky BP (*lower value*) from the INS^{+} experiment to the control run. All fluxes are in W m^{-2}, the relative changes are given for 127–125 and 116–114 ky BP as well. Anomalies that are not significantly different from the control run ($\alpha = 0.01$) are printed in italics. Positive numbers indicate an enhancement in the direction of the *arrow*

experiments covering the entire last interglacial were performed with a complex earth system model. Comparable experiments were so far only performed with intermediate complexity models.

The newly calculated vegetation and tree fraction differ substantially from the original input as used for the ECHAM3 atmosphere general circulation model. This bias is related to the difference between the observed vegetation as was used for ECHAM3 and the present-potential vegetation as modelled in this earth system model. However, the control run with interactive land surface did not differ widely in albedo values and climate from the control run with prescribed ECHAM3 parameters.

Climate change during the Eemian was forced by changes in the spatial and temporal patterns of incoming solar radiation. It caused clear changes in the land surface cover, especially in the high latitudes of the northern hemisphere, and in the monsoon regions in the subtropics of the northern hemisphere.

For the period from 128 to 120 ky BP, the simulated tree fraction in the high latitudes is larger than in the control run, with a maximum around 126 ky BP and a gradual decrease afterwards. Due to the positive feedback between temperature, forest growth and albedo, the decrease of forest area during the insolation experiments causes an increase of the surface albedo and enhances the temperature decrease in the high latitudes. A comparison between experiments with fixed land surface and experiments with interactive land surface shows that roughly two-thirds of this enhancement are due to the effect of forest presence on snow albedo, and one-third is due to the difference in background albedo between trees and grasses and due to synergetic effects between these two processes.

The enhanced monsoon circulation between 128 and 122 ky BP compared to the present situation over North Africa and Southeast Asia causes an increase in transport of water vapour to these regions. The enhanced vegetation growth and increase in soil moisture amplify this effect. The changes in the surface albedo are by far the most important parameter for this positive feedback between climate and land surface.

Overall, these changes in the land surface at high northern latitudes and in the northern hemisphere monsoon belt (in both cases related to changes in the surface albedo), have global implications, and tend to intensify climate change as induced by changes in the earth's orbit. This intensification was simulated for key climate factors, such as temperature and precipitation. Our simulations show no areas with a clear negative feedback on land surface albedo. The amplification due to albedo changes was simulated for the Eemian before by Kubatzki et al. (2000) and Crucifix and Loutre (2002). Together with albedo changes from ice sheet and sea ice changes, land surface albedo

could play a major role in the difference between glacial and interglacial climate, and might be an important factor in triggering the transition from an interglacial to a glacial, as was suggested before by de Noblet et al. (1996), Gallimore and Kutzbach (1996) and Yoshimori et al. (2002). Calov et al. (2005) however showed for the CLIMBER–2 model that vegetation dynamics are amplifying the feedback, but that changes in insolation, together with the feedback between ice cover, surface albedo and temperature, are capable of starting glaciation without vegetation dynamics, ocean dynamics or CO_2 decrease as essential trigger.

Probably the largest caveat of the experiment setup for a realistic reconstruction of Eemian climate is the absence of dynamical continental ice sheets. Over the time covered by the experiments (128–113 ky BP), the ice sheets are known to have changed (Tarasov and Peltier 2003), with a clear onset of glaciation towards the end of the covered period. Experiments with the ice sheet model SICOPOLIS (Greve 1997) are planned with an improved version of the coupled earth system model as presented in Winguth et al. (2005) and Mikolajewicz et al. (2007). Ice sheet changes are expected to enhance the albedo effect in high latitudes. In this way, the albedo changes due to ice sheets and vegetation changes might be an important factor for the onset of glaciation.

The acceleration of eight times, as used in the accelerated experiments, seems to be reasonable for assessing the effect of biogeophysical land surface changes, and much smaller differences were simulated between the experiments with and without acceleration of the insolation changes ($AINS^+$ and INS^+) than between the experiments with and without interactive land surface ($AINS^+$ and $AINS^-$). This indicates that the acceleration effect is much smaller than the effect of an interactive land surface. However, the use of the acceleration technique would not be appropriate for slower processes, e.g. carbon storage in soils or in the ocean. The acceleration would cause an artificial delay in the response, thereby mixing this delayed response with the timely signal of faster processes. For these purposes only unaccelerated experiments should be used.

Acknowledgments This work was performed in the CLIMCYC project, funded by the DEKLIM program of the German Ministry of Education and Research (BMBF). We would like to thank Martin Claussen and two anonymous reviewers for helpful comments.

References

Berger AL (1978) Long-term variations of daily insolation and quaternary climate change. J Atmos Sci 35:2362–2367

Bonan GB, Pollard D, Thompson SL (1992) Effects of boreal forest vegetation on global climate. Nature 359:716–718

Braconnot P, Joussaume S, Marti O, De Noblet N (1999) Synergistic feedbacks from ocean and vegetation on the African monsoon response to Mid-Holocene insolation. Geophys Res Lett 26:2481–2484

Brovkin V, Bendtsen J, Claussen M, Ganopolski A, Kubatzki C, Petoukhov V, Andreev A (2002) Carbon cycle, vegetation, and climate dynamics in the Holocene: experiments with the CLIMBER-2 model. Global Biogeochem Cycles 16:1139, doi:10.1029/2001GB001662

Calov R, Ganopolski A, Petoukhov V, Claussen M, Brovkin V, Kubatzki C (2005) Transient simulation of the last glacial inception. Part II: sensitivity and feedback analysis. Clim Dyn 24:563–576, doi:10.1007/s00382-005-0008-5

Charney JG (1975) Dynamics of deserts and droughts in the Sahel. Q J R Meteorol Soc 101:193–202

Charney J, Stone PH, Quirk WJ (1975) Drought in the Sahara: a biogeophysical feedback mechanism. Science 187:434–435

Charney JG, Stone PH, Quirk WJ (1976) Reply to Ripley EA, drought in the Sahara: insufficient biogeophysical feedback. Science 191:100–102

Claussen M (1991) Estimation of areally-averaged surface fluxes. Bound Lay Meteorol 54:387–410

Claussen M (1994) On coupling global biome models with climate models. Clim Res 4:203–221

Claussen M (1997) Modelling bio-geophysical feedback in the African and Indian monsoon region. Clim Dyn 13:247–257

Claussen M (1998) On multiple solutions of the atmosphere–vegetation system on present-day climate. Global Change Biol 4:549–559

Claussen M, Gayler V (1997) The greening of the Sahara during the mid-Holocene: results of an interactive atmosphere-biome model. Global Ecol Biogeogr 6:369–377

Claussen M, Lohmann U, Roeckner E, Schulzweida U (1994) A global data set of land-surface parameters. Max Planck Institute for Meteorology, Rep 135, Hamburg

Claussen M, Kubatzki C, Brovkin V, Ganopolski A, Hoelzmann P, Pachur HJ (1999) Simulation of an abrupt change in Saharan vegetation in the mid-Holocene. Geophys Res Lett 24:2037–2040

Claussen M, Mysak LA, Weaver AJ, Crucifix M, Fichefet T, Loutre MF, Weber SL, Alcamo J, Alexeev VA, Berger A, Calov R, Ganopolski A, Goosse H, Lohmann G, Lunkeit F, Mokhov II, Petoukhov V, Stone P, Wang Z (2002) Earth system models of intermediate complexity: closing the gap in the spectrum of climate system models. Clim Dyn 18:579–586

Coe MT, Bonan GB (1997) Feedbacks between climate and surface water in northern Africa during the middle Holocene. J Geophys Res 102:11087–11101

Crowley TJ, Baum SK (1997) Effect of vegetation on an ice age climate model simulation. J Geophys Res 102:16463–16480

Crucifix M, Loutre MF (2002) Transient simulations over the last interglacial period (126–115 kyr BP): feedback and forcing analysis. Clim Dyn 19:417–433

Crucifix M, Betts RA, Hewitt CD (2005) Preindustrial-potential and Last Glacial Maximum global vegetation simulated with a coupled climate-biosphere model: Diagnosis of bioclimatic relationships. Glob Planet Change 45:295–312

Diffenbaugh NS, Sloan LC (2002) Global climate sensitivity to land surface change: The Mid Holocene revisited. Geophys Res Lett 29:114. doi:10.1029/2002GL014880

DKRZ (1993) The ECHAM3 atmospheric general circulation model. Deutsches Klimarechenzentrum, Rep 6, Hamburg

Douville H, Royer JF (1997) Influence of the temperate and boreal forests on the Northern Hemisphere climate in the Météo-France climate model. Clim Dyn 13:57–74

Eltahir EAB (1996) Role of vegetation in sustaining large-scale atmospheric circulations in the tropics. J Geophys Res 101:4255–4268

Eltahir EAB, Gong C (1996) Dynamics of wet and dry years in West Africa. J Clim 9:1030–1042

Foley JA, Kutzbach JE, Coe MT, Levis S (1994) Feedbacks between climate and boreal forests during the Holocene epoch. Nature 371:52–54

Gallimore RG, Kutzbach JE (1996) Role of orbitally induced changes in tundra area in the onset of glaciation. Nature 381:503–505

Gallimore R, Jacob R, Kutzbach J (2005) Coupled atmosphere–ocean-vegetation simulations for modern and mid-Holocene climates: role of extratropical vegetation cover feedbacks. Clim Dyn 25:755–776. doi:10.1007/s00382–005-0054-z

Greve R (1997) Application of a polythermal three-dimensional ice sheet model to the Greenland Ice Sheet: response to steady-state and transient climate scenarios. J Clim 10:901–918

Hagemann S, Botzet M, Dümenil L, Machenhauer B (1999) Derivation of global GCM boundary conditions from 1 km land use satellite data. Max Planck Institute for Meteorology, Rep 289, Hamburg

Kubatzki C, Montoya M, Rahmstorf S, Ganopolski A, Claussen M (2000) Comparison of the last interglacial climate simulated by a coupled global model of intermediate complexity and an AOGCM. Clim Dyn 16:799–814

Kukla G, Robinson D (1980) Annual cycle of surface albedo. Mon Weather Rev 108:56–68

Levis S, Foley JA, Pollard D (1999) CO_2, climate, and vegetation feedbacks at the Last Glacial Maximum. J Geophys Res D24:31191–31198

Levis S, Foley JA, Pollard D (2000) Large-scale vegetation feedbacks on a doubled CO_2 climate. J Clim 13:1313–1325

Lorenz SJ, Lohmann G (2004) Acceleration technique for Milankovitch type forcing in a coupled atmosphere–ocean circulation model: method and application for the Holocene. Clim Dyn 23:727–743. doi:10.1007/s00382-0040469-y

Maier-Reimer E (1993) Geochemical cycles in an ocean general circulation model. Preindustrial tracer distributions. Global Biogeochem Cycles 7:645–677

Mikolajewicz U, Voss R (2000) The role of the individual air–sea flux components in CO_2 induced changes of the ocean's circulation and climate. Clim Dyn 16:627–642

Mikolajewicz U, Gröger M, Maier-Reimer E, Schurgers G, Vizcaíno M, Winguth AME (2007) Long-term consequences of anthropogenic CO_2 emissions simulated with a complex earth system model. Clim Dyn. doi:10.1007/s00382-006-0204-y (in press)

Milly PCD, Shmakin AB (2002) Global modeling of land water and energy balances. Part I: the land dynamics (LAD) model. J Hydrometeorol 3:283–299

de Noblet NI, Prentice IC, Joussaume S, Texier D, Botta A, Haxeltine A (1996) Possible role of atmosphere-biosphere interactions in triggering the last glaciation. Geophys Res Lett 23:3191–3194

de Noblet-Ducoudré N, Claussen M, Prentice C (2000) Mid-Holocene greening of the Sahara: first results of the GAIM 6000 year BP experiment with two asynchronously coupled atmosphere/biome models. Clim Dyn 16:643–659

Otterman J, Chou MD, Arking A (1984) Effects of nontropical forest cover on climate. J Clim Appl Meteorol 23:762–767

Preisendorfer RW (1988) Principal component analysis in meteorology and oceanography. In: Developments in atmospheric science, vol 17. Elsevier, New York, p 425

Prentice IC, Webb T III (1998) BIOME 6000: reconstructing global mid-Holocene vegetation patterns from palaeoecological records. J Biogeogr 25:997–1005

de Ridder K (1998) The impact of vegetation cover on Sahelian drought persistence. Bound Lay Meteorol 88:307–321

Roeckner E, Arpe K, Bengtsson L, Brinkop S, Dümenil L, Esch M, Kirk E, Lunkeit F, Ponater M, Rockel B, Sausen R, Schlese U, Schubert S, Windelband M (1992) Simulation of the model physics and resolution. Max Planck Institut für Meteorology, Hamburg, Report no 93

Sausen R, Voss R (1996) Techniques for asynchronous and periodically synchronous coupling of atmosphere and ocean models. Part I: general strategy and application to the cyclo-stationary case. Clim Dyn 12:313–323

Schurgers G, Mikolajewicz U, Gröger M, Maier-Reimer E, Vizcaíno M, Winguth A (2006) Dynamics of the terrestrial biosphere, climate and atmospheric CO2 concentration during interglacials: a comparison between Eemian and Holocene. Clim Past 2:205–220

Sitch S, Smith B, Prentice IC, Arneth A, Bondeau A, Cramer W, Kaplan JO, Levis S, Lucht W, Sykes MT, Thonicke K, Venevsky S (2003) Evaluation of ecosystem dynamics, plant geography and terrestrial carbon cycling in the LPJ dynamic global vegetation model. Global Change Biol 9:161–185

Tarasov L, Peltier WR (2003) Greenland glacial history, borehole constraints, and Eemian extent. J Geophys Res 108:2143. doi:10.1029/2001JB001731

TEMPO (Kutzbach JE, Bartlein PJ, Foley JA, Harrison SP, Hostetler SW, Liu Z, Prentice IC, Webb T III) (1996) Potential role of vegetation feedback in the climate sensitivity of high-latitude regions: a case study at 6000 years BP. Global Biogeochem Cycles 10:427–436

Texier D, De Noblet N, Harrison SP, Haxeltine A, Jolly D, Joussaume S, Laarif F, Prentice IC, Tarasov P (1997) Quantifying the role of biosphere–atmosphere feedbacks in climate change: coupled model simulations for 6000 years BP and comparison with palaeodata for northern Eurasia and northern Africa. Clim Dyn 13:865–882

Thomas G, Rowntree P (1992) The boreal forests and climate. Q J R Meteorol Soc 118:469–497

Voss R, Mikolajewicz U (2001) The climate of 6000 years BP in near-equilibrium simulations with a coupled AOGCM. Geophys Res Lett 28:2213–2216

Wilson MF, Henderson-Sellers A (1985) A global archive of land cover and soils data for use in general circulation climate models. J Climatol 5:119–143

Winguth A, Mikolajewicz U, Gröger M, Maier-Reimer E, Schurgers G, Vizcaíno M (2005) CO_2 uptake of the marine biosphere: feedbacks between the carbon cycle and climate change using a dynamic earth system model. Geophys Res Lett 32:L23714. doi:10.1029/2005GL023681

Yoshimori M, Reader MC, Weaver AJ, McFarlane NA (2002) On the causes of glacial inception at 116 kaBP. Clim Dyn 18:383–402